E Optical matters

E.1 The parabolic approximation

In this section we consider the parabolic approximation (PA) for rays through the inhomogeneous refractive index field resulting from heating with the gold plate.

E.1.1 Conditions for the parabolic approximation

In the PA, the assumption is that along the path of a ray the refractive index gradient (and with that the density gradient) does not change. In fig. 4.4 on page 47 we see the path of a ray through a sample of length L with a density gradient in the z-direction. In order to find the actual path of this ray, we turn to eq. (4.5) by which the path is determined in an inhomogeneous field:

$$\frac{d^2z}{dx^2} = \left\{ 1 + \left(\frac{dz}{dx}\right)^2 \right\} \frac{1}{n}\frac{dn}{dz}.$$

(E.1)

When along the path of a ray inside the sample ($0 \leq x \leq L$)

$$C_1 \equiv \left(\frac{dz}{dx}\right)^2 \ll 1$$

(E.2)

and, besides the change in the refractive index gradient, the change in the refactive index n itself is relatively small, so that

$$C_2 \equiv \left| \frac{\left(\frac{1}{n}\frac{dn}{dz}\right)_{x=L} - \left(\frac{1}{n}\frac{dn}{dz}\right)_{x=0}}{\left(\frac{1}{n}\frac{dn}{dz}\right)_{x=0}} \right| \ll 1 \,,$$

(E.3)

we arrive at the well known relation for the path of a light ray in the PA [103], for a ray entering parallel to the heater ($\left(\frac{dz}{dx}\right)_{x=0} = 0$) at height z_0:

$$z - z_0 = \left(\frac{1}{n}\frac{dn}{dz}\right)_{z_0} \frac{1}{2} x^2 \tag{E.4}$$

and

$$\frac{dz}{dx} = \left(\frac{1}{n}\frac{dn}{dz}\right)_{z_0} x. \tag{E.5}$$

Both conditions (E.2) and (E.3) determine the experimental circumstances for which the PA is valid.

To derive the values for C_1 and C_2 for specific experimental circumstances, i.e. distance to CP and input power density, we consider both values in terms of the density gradient. Because the density gradient is most large nearer to the heater, we may write:

$$C_1 \leq \left(\frac{L}{n}\frac{dn}{d\rho}\right)^2 \left(\frac{d\rho}{dz}\right)^2_{z=z_0}. \tag{E.6}$$

Out of the temperature field near the heater as described by eq. (2.38) and the relation (2.57) it is found that

$$\left(\frac{d\rho}{dz}\right)_z = \frac{\rho \alpha_p}{\lambda} \frac{q_f}{S_h} \operatorname{erfc}\left(\frac{z}{2\sqrt{D_T t}}\right), \tag{E.7}$$

out of which the density gradient at $z = z_0$ can be found. As an example, in fig. E.1, C_1 is displayed versus the distance to T_c for a ray entering at 100 μm from the heater, for power densities of 0.2 and 0.5 W/m^2 after heating for 60 seconds.

Figure **E.1** C_1 vs temperature for two different power densities.
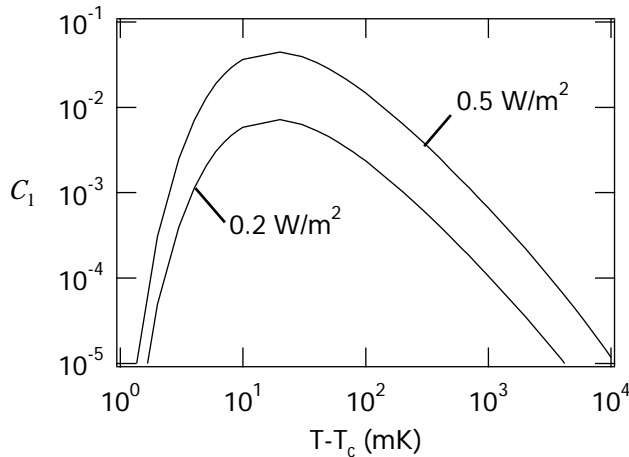
We see that for all temperatures, at distances of at least 100 μm from the heater and within 60 seconds, condition (E.2) is met when the power density is below 0.2 W/m^2. For power densities up to 0.5 W/m^2, it seems that between 5 and 100 mK from T_c one has to be careful in interpreting the results for distances as close as 100 μm from the heater.

To find C_2 for specific experimental circumstances, utilizing eq. (E.7) we may write

$$C_2 = \left| \frac{\mathrm{erfc}\left(\dfrac{z_{x=L}}{2\sqrt{D_T t}}\right)}{\mathrm{erfc}\left(\dfrac{z_0}{2\sqrt{D_T t}}\right)} - 1 \right|. \tag{E.8}$$

In order to find the density gradient at $x = L$, we need to find the distance to the heater, z_L, at which the ray leaves the cell. With eq. (E.4) we find:

$$z_L - z_0 = \frac{L^2}{2nd\rho}\frac{dn}{d\rho}\left(\frac{d\rho}{dz}\right)_{z_0}. \tag{E.9}$$

As an example, in fig. E.2, a contour plot of C_2 is displayed versus the distance to T_c and versus the entrance distance to the heater z_0 of a ray. The power density in this example is 0.5 W/m^2 and the time after the onset of heating is 60 seconds.

Figure   E.2   A contour plot of C_2.
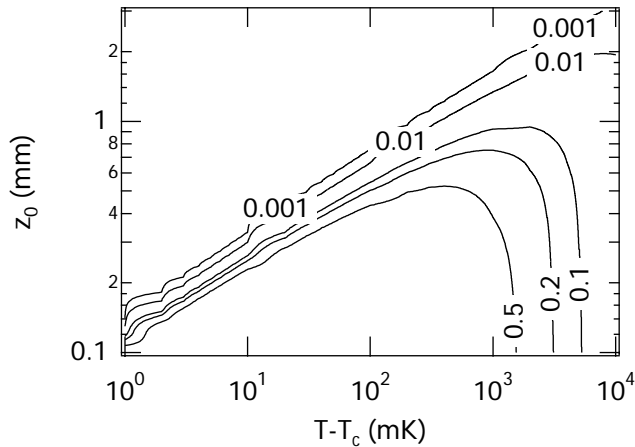
We see that in these experimental circumstances condition (E.3) is not always met. For rays entering closer than ±200 μm from the heater for almost the complete temperature range the PA is not explicitly applicable.

In regards to the 'shadow', we look at conditions (E.2) and (E.3) for the ray that determines its size in the PA (entering the sample at height $z = z_f$). For this specific ray, these conditions amount to:

$$C_1 = \left(\frac{L}{n}\frac{dn}{d\rho}\frac{d\rho}{dz}\right)^2_{z=z_f} \ll 1 \tag{E.10}$$

and

$$C_2 = \left| \frac{\text{erfc}\left(\dfrac{z_f + \Delta z}{2\sqrt{D_T t}}\right)}{\text{erfc}\left(\dfrac{z_f}{2\sqrt{D_T t}}\right)} - 1 \right| \ll 1 \, , \qquad (E.11)$$

where Δz is the distance that the ray travels inside the fluid in the z-direction. In the PA this distance, Δz_{PA}, is (eq. (E.4)):

$$\Delta z_{PA} = \left(\frac{1}{n}\frac{dn}{dz}\right)_{z_f} \frac{L^2}{2} \, . \qquad (E.12)$$

In fig. E.3, both C_1 and C_2 are displayed for the rays that determine the size of the shadow in the PA, z_f, at 5 different temperatures in a wide range above T_c, i.e. at 1, 10, 100, 1000 and 3000 mK from T_c. The curves higher in the graph correspond to temperatures further away from T_c. It is seen directly that, for these rays, the first condition is satisfied but the second not quite, implying that the paths of these rays do not follow the PA to a desired accuracy.

**Figure   E.3** C_1 and C_2 in time for z_f at various temperatures.
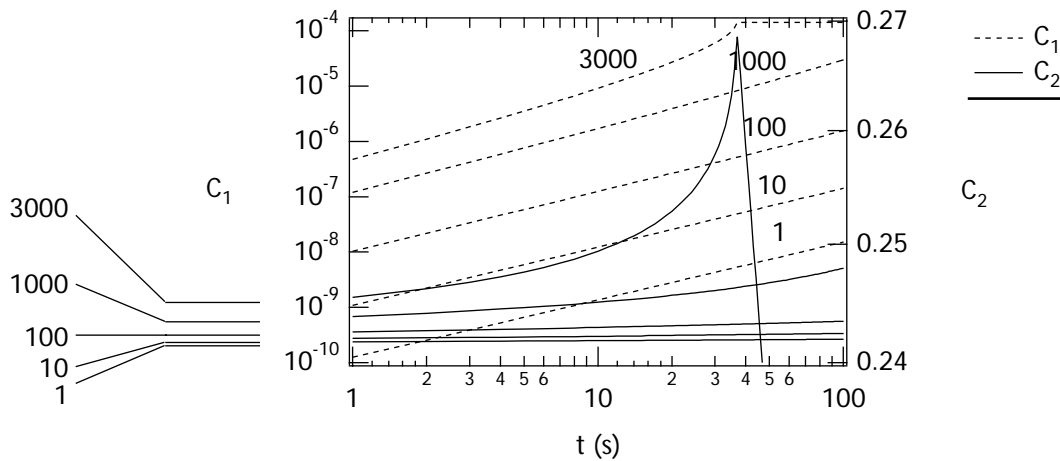
E.1.2   The accuracy of the parabolic approximation

In this section we calculate the accuracy of the PA in predicting the position in the film plane of a ray traveling through the inhomogeneous density field following linear heating.

We consider the path of a ray in an inhomogeneous density field following linear heating. Since in such a density field the refractive index gradient will always decrease along the path of a ray (it bends away from the heater), the real path will be less deviated and will exit the fluid under a smaller angle (w.r.t. the heater) than in the case of the PA. In fig. E.4 the real path and the path in the PA are sketched, displaying that the real exit angle ϑ is smaller than the exit angle in the PA, ϑ_{PA}. Furthermore, as shown in this figure, the virtual path inside the fluid of the real path crosses the middle of the sample a distance Δz_m further away from the heater than the entrance height of the ray. In the image plane of the mirror the position of the ray will be different accordingly and, to calculate its position in the film plane, it is the height of this virtual crossing which replaces the entrance height of the ray, as represented in eq. (4.16).

Figure **E.4** Schematic representation of the real path of a ray through the fluid compared to the path in the PA.
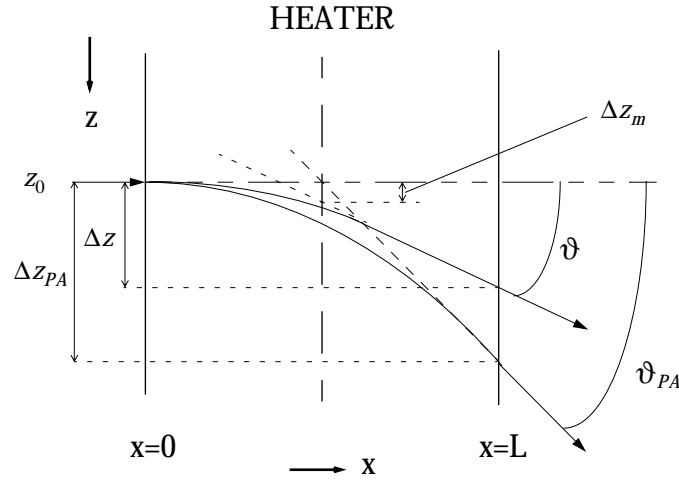
In order to determine the accuracy of the PA, we first write

$$z' = z'_{PA} - \Delta z' , \tag{E.13}$$

where, according to eq. (4.14) and (4.16),

$$z'_{PA}(z, t) = Mz(t) + FNLg_{n, PA}(z, t) , \tag{E.14}$$

$$\Delta z'(z, t) \equiv FNL[g_{n, PA}(z, t) - g_n(z, t)] - M \Delta z_m(z, t) \tag{E.15}$$

and

$$g_{n, PA}(z, t) = \left(\frac{1}{n}\frac{dn}{dz}\right)_z (t) . \tag{E.16}$$

When the path of a ray is approximated by the PA, the error in the calculation of the position in the film plane then is determined by the ratio

$$\frac{\Delta z'}{z'_{PA}} . \tag{E.17}$$

When $g_n(z, t)$ and $\Delta z_m(z, t)$ are approximated by eqs. (4.13) and (4.17), one finds

$$\Delta z'(z, t) = M\left(-\frac{1}{n^2}\frac{dn}{dz}\frac{d^2n}{dz^2}\right)_{z_0}\left[\frac{1}{6}\frac{FN}{M}L^3 - \frac{1}{24}L^4\right]. \tag{E.18}$$

Not surprisingly, in the parabolic approximation $\Delta z' = 0$.

For a density field following linear heating, by applying eqs. (4.21) and (4.22) one finds after some algebra

$$\Delta z'(z, t) = \frac{MZ_0}{24\sqrt{\tilde{t}}}\mathrm{erfc}\left(\frac{\tilde{z}}{2}\sqrt{\frac{\pi}{\tilde{t}}}\right)\exp\left(-\frac{\pi}{4}\frac{\tilde{z}^2}{\tilde{t}}\right)\left[4\frac{ML}{FN} - \left(\frac{ML}{FN}\right)^2\right], \tag{E.19}$$

where $\tilde{t} \equiv t/t_m$ and $\tilde{z} \equiv z/Z_0$. We see that for both optical layouts (CCD camera and Minolta) $\Delta z'(z,t) > 0$, since $(ML)/(FN) < 4$ (for $F < 0$ $Z_0 < 0$). The ratio of (E.17) then is:

$$\frac{\Delta z'}{z'_{PA}} = \frac{\dfrac{1}{24\sqrt{\tilde{t}}}\exp\left(-\dfrac{\pi}{4}\dfrac{\tilde{z}^2}{\tilde{t}}\right)\mathrm{erfc}\left(\dfrac{\tilde{z}}{2}\sqrt{\dfrac{\pi}{\tilde{t}}}\right)\left[4\dfrac{ML}{FN} - \left(\dfrac{ML}{FN}\right)^2\right]}{\tilde{z} + \mathrm{erfc}\left(\dfrac{\tilde{z}}{2}\sqrt{\dfrac{\pi}{\tilde{t}}}\right)} \qquad (E.20)$$

In fig.E.5 a contour plot of $\Delta z'/z'_{PA}$ is displayed versus the reduced values $\tilde{z}$ and $\tilde{t}$. From this plot we can conclude that, much as expected, the PA is more accurate further away from the heater ($z = 0$). This plot also shows that for a ray entering at a specific height z_0, the accuracy of the PA depends on the time, with a maximum at a time dependent on z_0.

Figure E.5 A contour plot of $\Delta z'/z'_{PA}$ versus z and t.
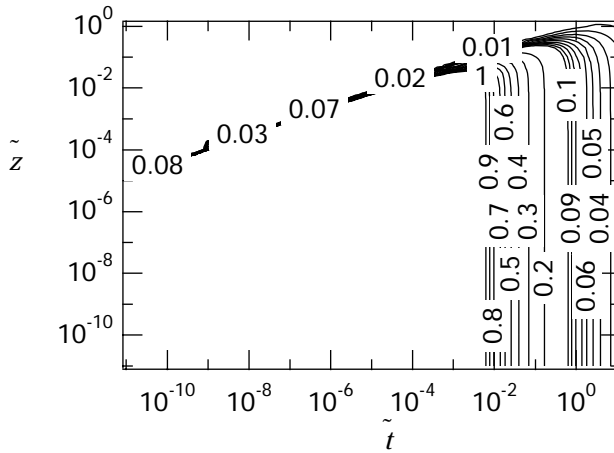
As a last step, we need to look at the rays $z_f(t)$ that determine the size of the shadow in time. When we apply eq. (4.24) in eq. (E.20) we find:

$$\frac{\Delta z'_f}{z'_f} = \frac{\left[\dfrac{1}{6}\dfrac{ML}{FN} - \dfrac{1}{24}\left(\dfrac{ML}{FN}\right)^2\right]}{1 + 2\sqrt{\dfrac{\tilde{t}}{\pi}}\dfrac{\sqrt{-\ln\sqrt{\tilde{t}}}}{\left(\sqrt{\phantom{\tilde{t}}}\sqrt{\tilde{t}}\right)}} \quad . \qquad (E.21)$$

In fig. E.6 the value of $\Delta z'_f/z'_f$ is displayed versus the reduced time $\tilde{t}$ for SF_6 and the CPF optical layout of the CCD camera. When we compare $\Delta z'_f/z'_f$ to the experimental accuracy in the determination of the shadow, which is in most cases of the order of percentages, fig. E.6 shows that for $t < t_m/100$ and for $t > 10 t_m$ the effect of the departure from the PA to the size of the shadow is negligible in comparison to the size calculated in the PA.

Figure   E.6   The effect of the departure from the PA to z_f in time.
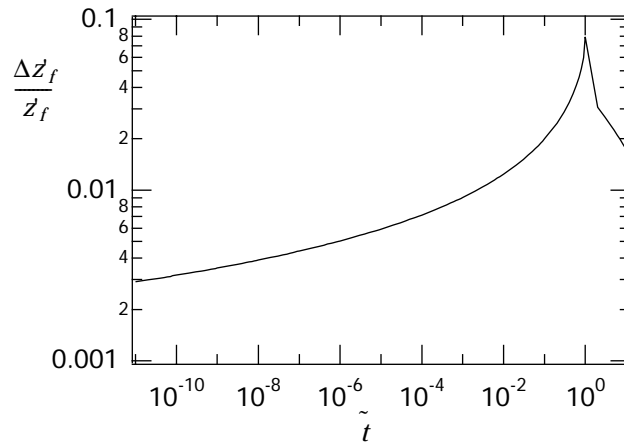
In terms of realistic heating times, power density and distance to T_c, looking at fig. E.6 and fig. 4.8, the result above suggests that for temperatures closer than about 100 mK from T_c the PA can be used safely in the determination of the size of the shadow. Up to 1 K from T_c the correctness of the PA heavily depends on the power density, where for even higher temperatures the shadow evaluation cannot be performed on the basis of the PA alone. Numerical simulations of the light paths through the fluid for a two-dimensional density field (including wall effects as described in section 4.2.3) support these conclusions.

E.2   CPF Optical details

Table   E.1   Optical layout for the CPF.

	M	F (mm)	N
CCD	1.404	60.87	1.341
Minolta	3.00	-263.38	0.69

Table   **E.2**   CPF Optical diagnostic methods.

CPF optical diagnostics	Visualisation	Attenuation	Interferometry (Twyman-Green)	SALS	WALS
Light source	LED light	He-Ne Laser 1 mW 0.6mm diam.	He-Ne Laser 0.6 mW.	He-Ne Laser 1 mW 0.6 mm diam.	He-Ne Laser 1 mW 0.6 mm diam.
Field of view (at object)	12 mm diam.	0.63 mm diam.	12 mm diam.	-	-
Detection Detector	CCD camera Photocamera	20 first pixels of SALS CCD	CCD camera Photocamera	Linear CCD (Peltier-cooled, 512 pixels)	Photomultiplier (1 angle at a time)
Angles	-	-	-	0°-30°	-22, -30, -38, 66, 74, 82, 90°, laser input ref., dark signal
Sensitivity		10^{-3}-10^{-7} W/pix.		10^{-6}-10^{-10} W/pix.	10^{-8}-10^{-12} W
Intensity resolution	6 bits/pixel (CCD digital downlink)	16 bits linear ($\approx$0.2%)	6 bits/pixel (CCD digital downlink)	8 bits (logarithmic) ($\approx$5.5%)	12 bits (logarithmic) ($\approx$0.35%)
Acquisition	30 fps	1 Hz or averaged	30 fps	1 Hz or averaged	Average over 300 ms per angle, 7 cycles/min
Downlink rate	30 fps & 1/6 Hz	1 Hz	30 fps & 16 Hz	1 Hz	7 cycles/min
Resolution (at object	40 µm (CCD) 20 µm (photoc.)	- -	Fringe density: 25 mm^{-1} (photoc.) 10 mm^{-1} (CCD)	0.25°	2°

Note: the SALS date are averaged over sets of four pixels before downlink